Advances in Radiation Oncology (2022) 7, 100987

advances in radiation oncology

www.advancesradonc.org

Scientific Article

CTV Delineation for High-Grade Gliomas: Is There Agreement With Tumor Cell Invasion Models?

Wille Häger,[a,b,*] Marta Lazzeroni,[a,b] Mehdi Astaraki,[b,c] and Iuliana Toma-Dașu[a,b]

[a]*Department of Physics, Stockholm University, Stockholm, Sweden;* [b]*Department of Oncology and Pathology, Karolinska Institute, Stockholm, Sweden;* [c]*Department of Biomedical Engineering and Health Systems, Royal Institute of Technology, Huddinge, Sweden*

Received March 16, 2022; accepted April 26, 2022

Purpose: High-grade glioma (HGG) is a common form of malignant primary brain cancer with poor prognosis. The diffusive nature of HGGs implies that tumor cell invasion of normal tissue extends several centimeters away from the visible gross tumor volume (GTV). The standard methodology for clinical volume target (CTV) delineation is to apply a 2- to 3-cm margin around the GTV. However, tumor recurrence is extremely frequent. The purpose of this paper was to introduce a framework and computational model for the prediction of normal tissue HGG cell invasion and to investigate the agreement of the conventional CTV delineation with respect to the predicted tumor invasion.

Methods and Materials: A model for HGG cell diffusion and proliferation was implemented and used to assess the tumor invasion patterns for 112 cases of HGGs. Normal brain structures and tissues as well as the GTVs visible on diagnostic images were delineated using automated methods. The volumes encompassed by different tumor cell concentration isolines calculated using the model for invasion were compared with the conventionally delineated CTVs, and the differences were analyzed. The 3-dimensional-Hausdorff distance between the CTV and the volumes encompassed by various isolines was also calculated.

Results: In 50% of cases, the CTV failed to encompass regions containing tumor cell concentrations of 614 cells/mm^3 or greater. In 84% of cases, the lowest cell concentration completely encompassed by the CTV was ≥1 cell/mm^3. In the remaining 16%, the CTV overextended into normal tissue. The Hausdorff distance was on average comparable to the CTV margin.

Conclusions: The standard methodology for CTV delineation appears to be inconsistent with HGG invasion patterns in terms of size and shape. Tumor invasion modeling could therefore be useful in assisting in the CTV delineation for HGGs.

Introduction

High-grade gliomas (HGG) is a group of brain cancers comprised of anaplastic astrocytoma (WHO grade III) and glioblastoma multiforme (GBM, WHO grade IV). Despite GBMs being the most common primary malignant brain cancer in adults, limited advancement in treatment has been made and prognosis remains poor.[1]

It is thought that the spread of clonogenic GBM cells far from the gross tumor volume (GTV) is responsible for the persistent tumor recurrence.[2] Microscopic tumor cell invasion around the GTV is conventionally handled by expanding the GTV into a clinical target volume (CTV). The CTV should by definition encompass all tumor cells. The methodology for delineating CTVs varies between tumor type and treatment modality, but generally consists

Sources of support: Financial support from the Swedish Cancer Research Funds of Radiumhemmet (RaHFo) and the Swedish Research Council (project registration number 2020-04618) is kindly acknowledged.

Disclosures: none.

Data sharing statement: Research data are available at: https://www.med.upenn.edu/cbica/brats2020/data.html.

*Corresponding author: Wille Häger; E-mail: wille.hager@fysik.su.se

https://doi.org/10.1016/j.adro.2022.100987

of adding a margin to the GTV contour while conforming the CTV contour to natural barriers.[3,4] For GBMs, tumor growth can reoccur centimeters away.[5–8] Standard methodology for GBM CTV delineation involves a GTV contour expansion by up to 3 cm,[9–11] but prognosis still remains poor. Meanwhile, the brain itself is a critical organ at risk, and the treated volume should ideally be as limited as possible. Histological studies have also shown that clonogenic glioma cells can exist up to 4 cm away from the visible GTV, and that the spread appears anisotropic,[12–14] explaining potentially why the standard CTV delineation for HGGs has been largely unsuccessful.

Mapping of the spatial distribution of clonogenic cells mostly relies on imaging by MRI. T1-weighted (T1) imaging has a reported detectability threshold of ~8000 cells/mm^3.[15] T2-weighted (T2) imaging may have a lower detectability threshold,[16] but may increase the visibility of peritumoral edema rather than the tumor itself.

Histopathological data on HGGs is scarce but the diffusive nature of HGG tumors along with the given MRI visibility threshold indicate that considerable volumes of brain tissue infiltrated by tumor cells may be invisible upon imaging. To provide information on tumor cell infiltration undetectable by imaging, many attempts at modelling HGG growth and invasion of normal tissue have been made.[17,18] The first models assumed isotropic growth,[15,19] but they have since evolved into more complex models that assume anisotropic growth,[16,20,21] and may account for growth along the white matter tracts as well as for morphological deformation.[22,23] While the methodology and complexity vary, some model assumptions are universally shared: the spread of the tumor is the result of diffusion and proliferation of GBM cells; GBM cells primarily spread in white matter rather than gray matter; GBM cells cannot cross natural barriers such as in-between brain folds, the longitudinal fissure, and ventricles; and the corpus callosum being the only link between the hemispheres.

However, the modelling of HGG growth and spread has not yet seen a clinical implementation. One problem hindering its translation to the clinic is the uncertainty of the model parameter values describing the diffusion and proliferation of GBM cells. HGG modelling mostly relies on rough estimates of the input parameters, which are often based on theoretical approximations and on the few available experimental values.[20,24–26] It is known that the growth rates of GBMs vary considerably,[27] but the normal tissue infiltration patterns are less established. Parameters lacking substantial evidence in their numerical values include the maximum acceptable tumor size to prevent gliomatosis cerebri, the normal tissue cell carrying capacity, as well as the MRI cell concentration visibility threshold. Nevertheless, modelling of HGG invasion may still be useful in assisting the delineation of the CTV, as has been shown by Unkelbach et al.[24] for a limited number of cases provided that correlation between model predictions and outcome can be determined. To the best of the authors' knowledge, this is the first study in which the CTV delineation of HGGs is compared to simulated tumor invasion for a large number of cases having various degrees of complexity.

The purpose of this paper is to introduce a framework for the prediction of HGG cell invasion in normal tissue, to implement it in a computational model, and to investigate the agreement of the conventional CTV delineation with respect to the predicted tumor invasion.

Material & Methods

A data set consisting of 126 GBM/HGG cases from the Brain Tumor Segmentation (BraTS) challenge 2020 was included in the study.[28-31] Four MRI scans, namely T1-weighted, postcontrast T1-weighted (T1-Gd), T2-weighted, and T2 fluid attenuated inversion recovery (FLAIR) were available. The image data set was preprocessed by the challenge organizer, that is, skull-stripped and registered to a 240 × 240 × 155 mm^3 template. Bias field corrections were applied to fix the intensity inhomogeneities in the MR images.

Because of the large amount of data, automatic delineation of tumor tissues and brain matter types was used. Based on the capability of deep convolutional autoencoders, a normal appearance autoencoder (NAA)[32,33] model was developed to capture the distribution of healthy anatomic brains from MRIs. To train the NAA model on a supervised fashion, synthetic paired images were generated so that the NAA model was forced to reconstruct tumor-free images from pathologic images. Residual images were calculated as the differences between the original tumoral data and the reconstructed tumor-free images and integrated into a U-Net-like network[34] as prior information to improve the segmentation performance. Segmentation masks were produced using all the MRI scans as input data for the NAA model. The segmentation masks were grouped as necrotic and nonenhancing tumor, peritumoral edema, Gd-enhanced tumor, and the background. The segmented GTV (V_0) was defined as the combined volume of the Gd-enhanced tumor volume and the necrotic tumor volume, $V_0 = V_{\text{Gd-enhanced}} \cup V_{\text{necrotic}}$.

An automated segmentation algorithm known as "Oxford Centre for Functional MRI of the Brain automated segmentation tool"[35] (FAST) with default settings was used to segment the T1 image into white matter, gray matter, and anatomic barriers. The algorithm did not segment regions of tumor tissue. Limitations in the ability of the algorithm to differentiate gray matter from barriers required some manual intervention: a region 9-voxel wide between the brain hemispheres was manually stripped of gray matter to ensure

that the longitudinal fissure remained intact as a barrier, and the corpus callosum, considered as the dominant pathway between the hemispheres, was enhanced to ensure a connection was present. Other pathways, for example, the optic tracts and commissures, were not explicitly accounted for.

Combining the artificial intelligence (AI) segmentation with the FAST segmentation yielded a brain segmented into white and gray matter, natural barriers, and the segmented GTV, V_0, which was assumed to have a peripheral cell concentration equal to or above the MRI visibility threshold of 8000 cells/mm^3.

Tumor invasion modeling

Tumor invasion was modelled using a Fisher-Kolmogorov equation (Eq. 1) from Murray et al.[15,19,36-38] The model employs a partial time differential equation with 1 term accounting for the tumor cell spread and 1 term accounting for the tumor cell proliferation. The time variation of cell concentration is:

$$\frac{\partial c(\mathbf{r},t)}{\partial t} = \nabla \cdot D(\nabla c(\boldsymbol{r},t)) + \rho c\left(1 - \frac{c(\mathbf{r},t)}{k}\right) \quad (1)$$

where $c(\mathbf{r},t)$ is the clonogenic cell concentration, which is a function of the space coordinate $\mathbf{r} = (x,y,z)$ and time, ρ is the proliferation factor, k is the normal tissue tumor cell carrying capacity, and $D = D(\mathbf{r})$ is the diffusion coefficient, which varies as:

$$D(\mathbf{r}) = \begin{cases} D_W & \text{for} \quad \mathbf{r} \in W \\ D_G & \text{for} \quad \mathbf{r} \in G \\ 0 & \text{elsewhere} \end{cases}. \quad (2)$$

where W and G are white matter and gray matter voxels, respectively. All voxels in V_0 were assigned as white matter to allow unhindered diffusion within the volume.

Eq. 1 was discretized and solved numerically using finite-difference time-domain methods and implemented in MatLab.[39] Before simulation, a tumor cell population (n_0) was placed in a 6-voxel large volume centered on the center-of-mass (COM) of V_0. This cell population accounts for the fact that tumors may grow until a certain cell number threshold before spreading away from the tumor bulk.[26] The simulation was iterated in time and each iteration consisted of a diffusion calculation followed by a proliferation calculation. The simulation ceased when all voxels of the V_0 contour had a cell concentration of at least 8000 cells/mm^3 (Fig 1). The simulated GTV (V) was defined as the new volume encompassed by the 8000 cells/mm^3 isosurface.

The initial tumor cell population and the normal tissue tumor cell carrying capacity were kept constant: n_0 equal to $1.5 \cdot 10^6$ cells and k equal to $2.39 \cdot 10^5$ cells/mm^3.[25,26]

Multiple simulations were run for different values of the following parameters:

1. D/ρ (mm^2) representing the capability of the tumor to diffuse into normal tissue, where a low value of D/ρ corresponds to a less diffusive tumor
2. D_W/D_G, characterizing the anisotropical growth of the tumor, where a large ratio corresponds to more anisotropic invasion of normal tissue

The volume V is therefore dependent on D/ρ and D_W/D_G:

$$V = V\left(\frac{D}{\rho}, \frac{D_W}{D_G}\right). \quad (3)$$

The range of values of the investigated parameters is given in Table 1. Tumor invasion was simulated for all combinations of parameters, resulting in 30 different tumor invasion patterns per patient case.

The ratios of V and V_0 were investigated (Fig 1). The parameters yielding the smallest volume of V were denoted as $(D/\rho)_{\text{opt}}$ and $(D_W/D_G)_{\text{opt}}$, and the volume itself was denoted as the optimal volume, V_{opt}:

$$V_{\text{opt}} = V\left(\left(\frac{D}{\rho}\right)_{\text{opt}}, \left(\frac{D_W}{D_G}\right)_{\text{opt}}\right) = \min\left(V\left(\frac{D}{\rho}, \frac{D_W}{D_G}\right)\right) \quad (4)$$

Thus, $(D/\rho)_{\text{opt}}$ and $(D_W/D_G)_{\text{opt}}$ are the parameters yielding the best match between V and V_0 for each patient case. The simulations of tumor invasion with optimal parameters were used as the basis for further analysis.

A CTV was created for each patient case by isotropically extending the segmented GTV contour by 20 mm within the brain. The CTV was confined to 1 brain hemisphere as determined by the COM of the segmented GTV, except for 6 cases of suspected butterfly GBM.[40] The agreement of the CTV delineation with the predicted tumor invasion was assessed in 2 ways:

1. By determining the lowest cell concentration isoline completely encompassed by the CTV (c_{enc})
2. By determining which cell concentration isoline yielded the lowest 3-dimensional Hausdorff distance, $d_H(c)$, compared with the CTV

Thus, c_{enc} represents the lowest cell concentration that is fully encompassed in the volume delineated by using the conventional CTV methodology, whereas $d_H(c)$ indicates the cell concentration that best conforms to the CTV. The range of input values of $d_H(c)$ investigated is given in Table 1. An ideal CTV should yield $c_{\text{enc}} \approx 0$ and $d_H(0) = 0$, indicating a delineation of the entire tumor cell

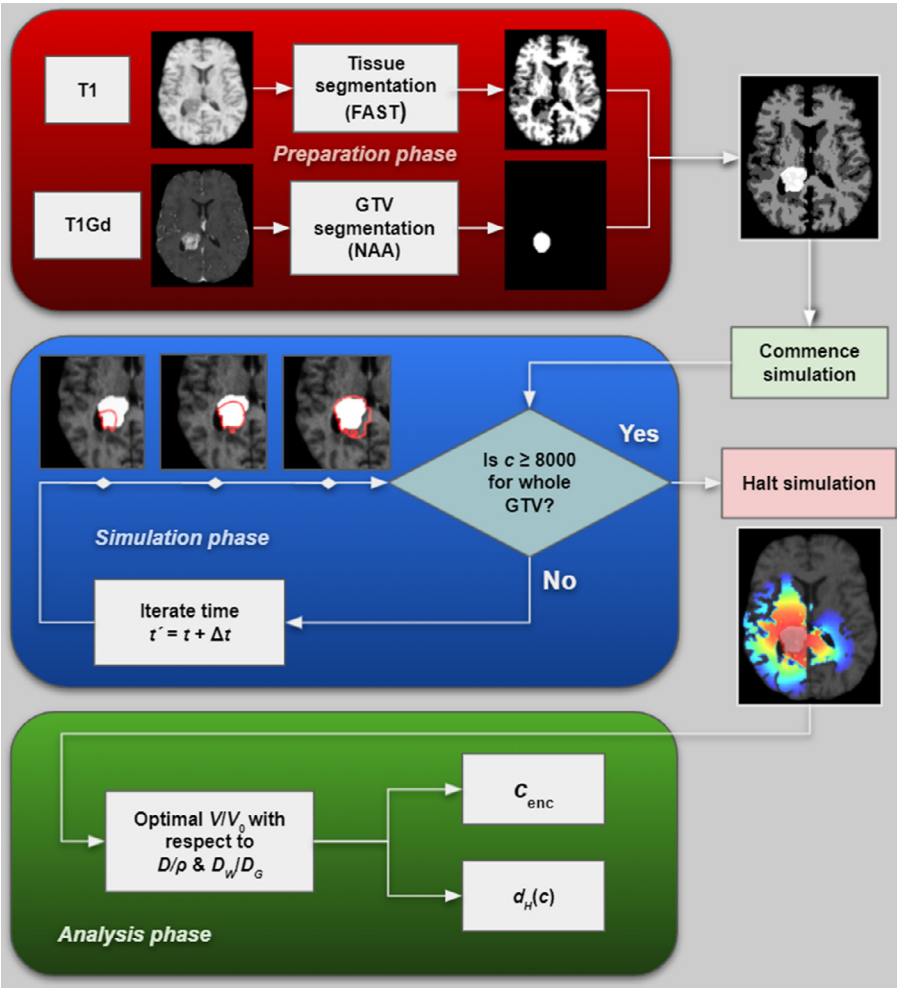

Fig. 1 Workflow of the study. The brain tissue types and GTVs are segmented in the preparation phase. Simulation is then commenced by placing an initial number of cells in the center-of-mass of the GTV. As the simulation is iterated with time, the tumor grows. The simulation is iterated until the halting condition of encompassing the entire GTV with a cell concentration ≥8000 cells/mm^3 is achieved. Multiple simulations with varying D/ρ and D_W/D_G are run for each case. The simulated GTV yielding the best match with the segmented GTV is then further analyzed. The lowest valued cell concentration isosurface that is completely encompassed by the clinical target volume delineation, c_{enc}, is determined, as well as the Hausdorff index, $d_H(c)$, of the volume encompassed by isosurface of cell concentration c and the clinical target volume. *Abbreviations:* FAST = FMRIB's automated segmentation tool; GTV = gross tumor volume; NAA = normal appearance autoencoder.

Table 1 Range of the parameters investigated in the study

D/ρ (mm^2)*	0.1	0.5	1.0	5.0	10.0	15.0	20.0	25.0	30.0	40.0
D_W/D_G†	10	100‡	1000							
$d_H(c=)$ (cells/mm^3)	10	50	100	200	400	800	2000	4000	8000	

Abbreviation: CTV = clinical target volume.
* Range based on values from Swanson et al.[42]
† Range partially based on estimations from Swanson et al.[16,20]
‡ Value used by Unkelbach et al.[24]
The parameters D/ρ and D_W/D_G correspond to tumor diffusiveness and invasion anisotropy, respectively, and $d_H(c)$ is the Hausdorff index of the volume encompassed by the isosurface of cell concentration, c, and the volume of the conventional CTV. All combinations of D/ρ and D_W/D_G were tested. The values for $d_H(c)$ were investigated using $(D/\rho)_{opt}$ and $(D_W/D_G)_{opt}$.

population with perfect conformity. A summary of the methodological workflow is shown in Figure 1.

Results

Simulated tumors exhibited preferential spread along the white matter, partial avoidance of gray matter, and complete avoidance of ventricles and folds. Some examples of the simulated tumor invasion are given in Figure 2. Typical cases presenting a good agreement between V_0 and V are shown in the upper panels (Fig 2a-c). Figure 2d shows a case with a segmented GTV located centrally in the brain. V extended beyond the CTV delineation and into the opposite hemisphere. Considerable tumor cell invasion beyond the CTV contour was observed. Figure 2e shows a case where V_0 is close to the periphery of the brain. In this case, V_0 was surrounded by edema, which was interpreted as gray matter by the segmentation algorithm. This confined the spread of V, thus resulting in good agreement between the volumes. The CTV delineation overextended beyond the tumor invasion. Figure 2f shows a case where V_0 consists of multiple volumes. Poor agreement between V and V_0 was observed, as V needed to extend beyond the primary tumor mass to encompass the smaller tumor mass. It should, however, be noted that the CTV appears to encompass V reasonably well. For 14 cases the segmented GTV was located close to the longitudinal fissure, creating the appearance of a connection between the 2 hemispheres where there normally should have been a barrier. These cases were discarded from the analysis because of this artefact.

Figure 3a shows a box plot of V_{opt}/V_0 for the 112 cases included in the study. The median value for V_{opt}/V_0 is 1.89 with a range (1.18, 6.18) and mean 2.35±1.15 (1σ). Fourteen cases (12.5%) were discarded from the analysis presented in Figure 3a because their V_{opt}/V_0 values were larger than the 1.5 interquartile range corresponding to $V_{opt}/V_0 > 6.6$ and thus classified as outliers. For 4 other cases (3.6%) the algorithm yielded $V_{opt}/V_0 < 1$, which was regarded as a simulation failure and hence further discarded. A closer analysis of these specific instances

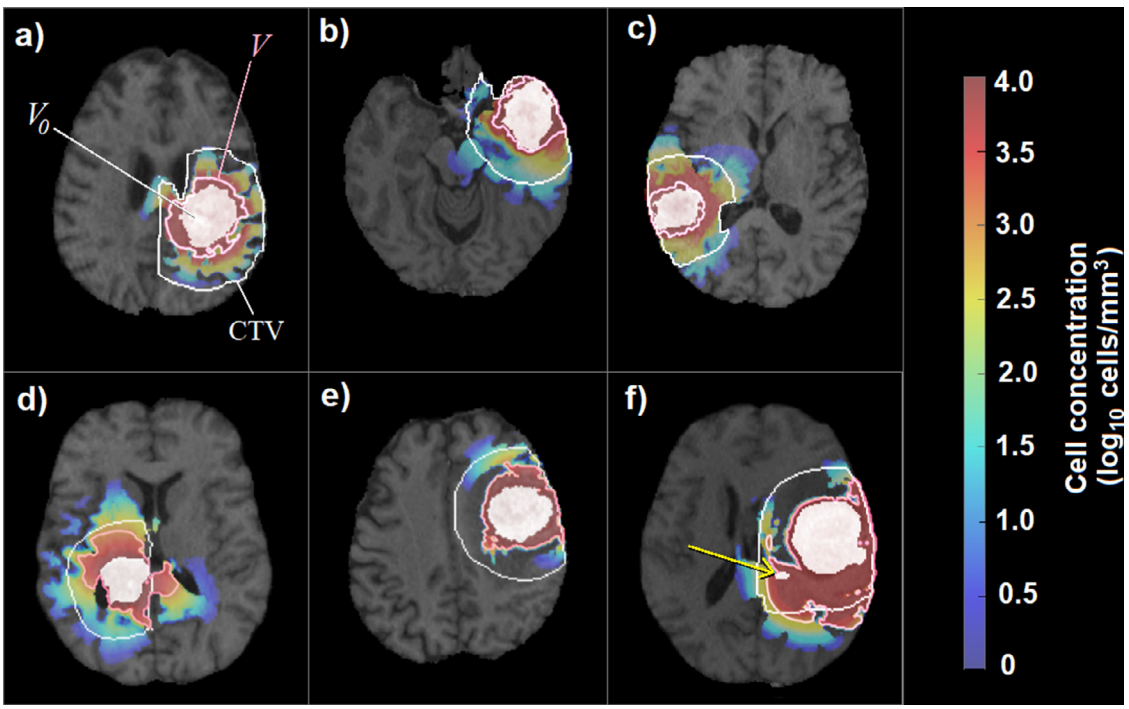

Fig. 2 Six examples of simulated tumor invasions. The white volumes correspond to the segmented gross tumor volumes (GTVs) (V_0), and the red volumes with pink margins correspond to the simulated GTVs (V). The full tumor extension is indicated by the color wash ($\log_{10}$). The white contour corresponds to the conventional clinical target volume (CTV), formed by expanding the segmented GTV margin by 20 mm while adhering to natural barriers and 1 hemisphere. Top row: A-C, Typical cases where good agreement between V_0 and V is observed. Bottom row D-F, Cases displaying atypical model behavior. D, The volume V_0 is close to the hemisphere barrier, and the simulated tumor has invaded the other hemisphere. There are considerable tumor cell concentrations outside the CTV. E, The volume V_0 is surrounded by edema, which is interpreted as gray matter, and there is agreement between V_0 and V. The CTV overextends the tumor. F, A case where V_0 consists of separated volumes. There is a primary bulk tumor mass and a smaller separated volume (yellow arrow). Here V is bordered by the smaller mass, indicating that the smaller volume was responsible for an extended simulation time.

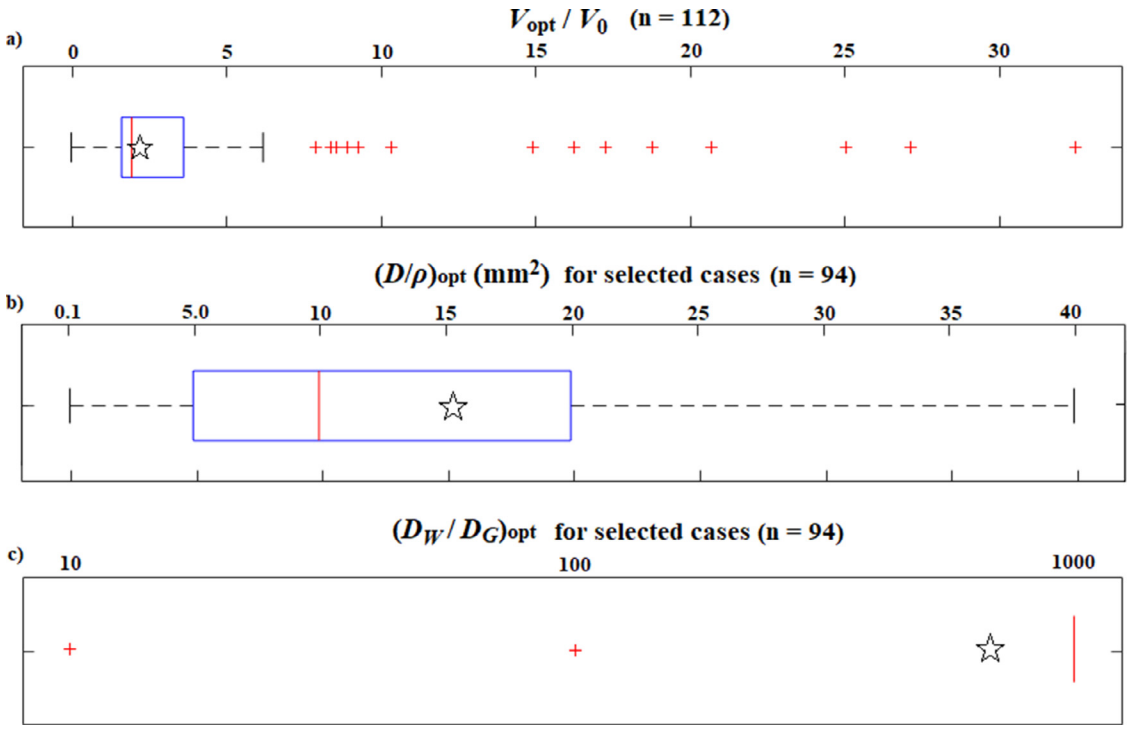

Fig. 3 Box plots with mean values (☆), median value (red stripe), and outliers (+) of: (a) V_{opt}/V_0; (b) $(D/\rho)_{opt}$; (c) $(D_W/D_G)_{opt}$.

indicates that they correspond to particular geometric conditions for the segmented GTV and/or extreme values for the simulation parameters, as explained in the Discussion section.

The mean, median, and range of values for the $(D/\rho)_{opt}$ and $(D_W/D_G)_{opt}$ for the remaining 94 selected cases are shown in Figures 3b and 3c, respectively. The means of $(D/\rho)_{opt}$ and of $(D_W/D_G)_{opt}$ were 15.14 mm^2 ± 88.2% and 810.4 ± 46.8%, respectively. The $(D/\rho)_{opt}$ values were found to cover the whole range of considered values, whereas $(D_W/D_G)_{opt}$ favored high values, with D_W/D_G = 10 and D_W/D_G = 100 deemed as outliers.

Figure 4a shows the values of the lowest cell concentration isoline completely enclosed by the CTV, c_{enc}, for all analyzed cases. The c_{enc} values covered the whole range from 0 cells/mm^3 to $2.39 \cdot 10^5$ cells/mm^3 (i.e., normal tissue tumor cell carrying capacity). Twelve out of 94 cases (12.8%) were deemed as outliers with $c_{enc} > 1.04 \cdot 10^4$ cells/mm^3 (>1.5 interquartile range). In 50% of cases, c_{enc} > 614 cells/mm^3, meaning that in 50% of the cases the CTV failed to encompass a cell concentration isoline smaller than this value. Cell concentration isolines are shown in Figure 4b for 1 exemplifying case having a c_{enc} equal to 22 cells/mm^3.

The median Hausdorff distance of the analyzed 94 cases did not vary significantly with cell concentration threshold, $d_H(c)$, although a trend appeared to indicate an initial decrease with increasing cell concentration threshold reaching the lowest value for a range of 100 to 200 cells/mm^3, corresponding to $d_H(c)$ = 19.72 mm, followed by an increase up to a maximum of $d_H(c)$ = 20.62 mm. This indicates that the simulated tumors, as defined by various isolines, did not conform to the CTV delineation because of their anisotropic spread.

Discussion

The CTV concept has been successful in the management of many tumors. For HGG, however, the isotropic expansion of the GTV as CTV may not be appropriate due to the preferential tumor cell migration through white matter over gray matter up to large distances from the observable border of the GTV. Tumor invasion modeling may therefore assist the CTV delineation. The anisotropic pattern of spread of HGG cells was clearly observed and visualized in this study, as was the difficulty in finding a volume encompassed by a tumor cell concentration isoline fully encompassed by the CTV without including also volumes of healthy tissue, when the conventional CTV delineation was used.

The value of the tumor cell concentration isoline fully encompassed by the CTV, c_{enc}, considered to be clinically acceptable may be treatment- and/or patient-dependent. Based strictly on the definition of CTV as the target that encompasses all tumor cells, the value of c_{enc} should ideally approach zero, but this may be an unrealistic goal for invasive tumors such as HGGs according to this model.

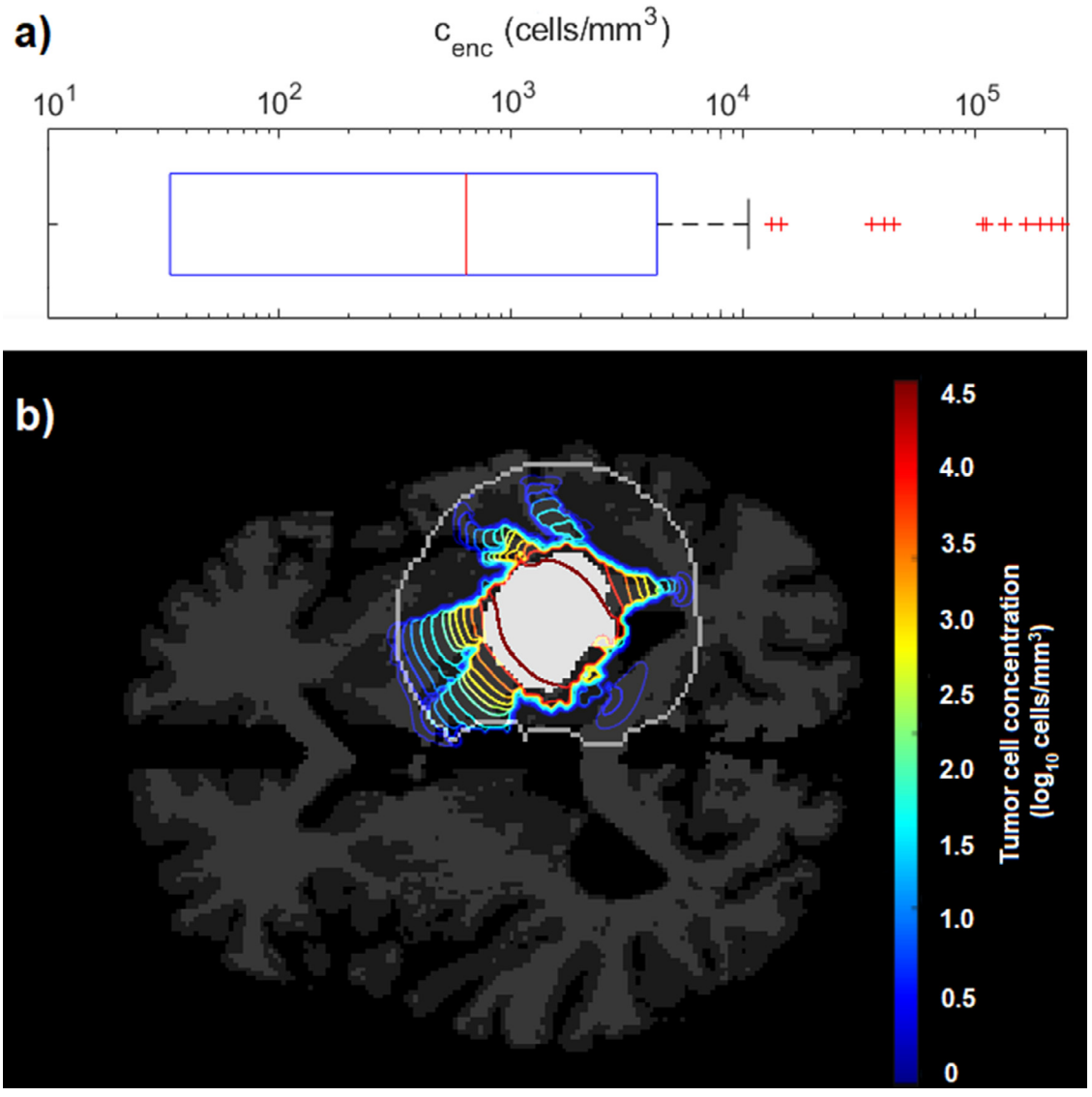

Fig. 4 (a) Box plot showing the distribution (median value and quartiles) of the lowest cell concentration isoline completely enclosed by the clinical target volume, c_{enc}, for all analyzed cases. The vertical striped line corresponds to 8000 cells/mm^3. One case where $c_{enc} = 0$ is not displayed. (b) An example of a simulated tumor cell concentration isoline, where $c_{an} = 22$ cells/mm^3. The segmented gross tumor volume (V_0) corresponds to the white mass and the conventional clinical target volume is outlined in white.

The values in this study were, therefore, arbitrarily chosen for discussion relative to the detectability limit by MRI. In 15% of cases when $c_{enc} > 8000$ cells/mm^3, the segmented GTVs were difficult to fully encompass because of, for example, multiple tumor volumes and large total volumes. For 50% of cases $c_{enc} > 614$ cells/mm^3. Recurrence of tumor growth would therefore not be surprising for such cases and the CTV delineation might benefit from model-based guidance.

The Hausdorff distance was on average comparable to the CTV extension of 20 mm for all isosurfaces. Because the morphology of the brain promotes anisotropic tumor invasion, the Hausdorff distance will always be in the same magnitude as the CTV extension distance.

Both analyses of c_{enc} and $d_H(c)$ indicate poor agreement between the CTV delineation and the simulated tumor invasion. Although the former shows that regions of considerable tumor cell concentrations are not covered by the CTV delineation, the latter shows that there is poor conformity. Both issues could potentially be improved by delineating CTVs that better conform to the white matter.

Modeling HGG invasion patterns has previously been performed.[15-23] Most studies have applied the same underlying model as in this work (Eq. 1) but used an alternative modality for solving it by assuming that the wave-front of the tumor invasion expands with a constant velocity.[24,41,42] This solution circumvents the need to fit a

simulated tumor volume with a segmented one, because the wave-front starts from the segmented tumor border. This contrasts with the method used in this study, which handles each voxel independently. The study by Unkelbach et al[24] used the wave-front solution to determine tumor invasion in 10 cases of GBM and compared the CTV delineations to the target volumes. However, a different target definition method was used: the CTV was contoured by extending the T2-FLAIR hyperintensity volume by 1 to 2 cm, and the target volume was defined as the tumor cell isoline with the same total volume as the CTV. The Dice similarity coefficients[43] revealed an average match of 79% with range (74, 84%). A direct comparison of the 2 studies cannot be performed because of the different definition of the target volume.

An alternative methodology for CTV delineation, based on extending the GTV margin a constant distance while accounting for all barriers, has also been suggested.[44] In a 15-year study covering 174 patients, Duma et al[45] used T2 FLAIR imagery to reportedly visualize the invasion patterns of GBM tumors, targeted the invasion pathways of the white matter tracts using radiosurgery, and reported a median survival of 23 months. This study therefore suggests that not only the delineation of the CTV but also the actual dose distribution could benefit from a better insight of the pattern of invasion of HGG cells into the brain.

The NAA model for tumor segmentation used in this study relied on all MRI scans as input data to maximize information. The model did not attempt to segment tumor invasion. For manual CTV delineation, previous studies have attempted to use T2-FLAIR as an indicator of tumor spread.[24,41,45] However, because T2-FLAIR highlights fluids such as peritumoral edema, the interpretation of T2-FLAIR hyperintense regions in terms of tumor infiltration of normal tissue is not straightforward. An alternative methodology for manual CTV delineation that does not rely on T2 scans but is based on extending the GTV margin by a constant distance while accounting for the anatomic barriers has also been suggested.[44]

Tumor and tissue segmentation was carried out in this study by AI methods and the FAST algorithm. The FAST algorithm was chosen for its availability and ease of use, but also because encouraging, positive results were previously reported.[46] However, the automated process had some limitations. Many cases included GTVs consisting of several disjunct subvolumes, some of which were the size of individual voxels. It is unknown whether such fragment volumes are artefacts of the automatic tumor delineation or not. Disregarding small tumor volumes separated from the primary tumor bulk would likely yield better agreement between V and V_0 because the simulation halting condition would be achieved easier. In case of compact V_0, V would not need to spread as far into normal tissue to encompass remote fragments, thus limiting the V/V_0 ratio.

The data used in this study came from the BraTS 2020 challenge intended for segmentation training. Some patients may therefore not have been eligible for radiation therapy or radiosurgery based on the size or location of the tumor. Delineating a CTV for such cases may therefore be regarded as a theoretical exercise with limited practical relevance or even as a source of bias of the results toward extreme values because of the inclusion of cases that would not be treated with radiation therapy. The tumor invasion modeling and the theoretical c_{enc} and $d_H(c)$ analyses would, however, not be affected.

The outcome of the model for invasion depends on the choice of its parameters. The approach considered in this paper for the choice of parameters was the determination of optimal ones with respect to the agreement between V and V_0 for individual cases. The value of $(D/\rho)_{\text{opt}}$ may therefore be influenced by simulation conditions such as the size, shape, and location of V_0, surrounding tissue types, and presence of the natural barriers. A large spread of $(D/\rho)_{\text{opt}}$ values was observed for different patients. Determining D/ρ values has been previously attempted by observing GTV growth over time and has also yielded a wide range of values (0.24, 35.92 mm^2).[41] GBMs appear to grow at different rates among patients,[27] but the reason for this and how this affects the cell spread is unclear. Additionally, D/ρ may also be time-dependent as cell proliferation may dominate in the early tumor growth stages but slow down as the tumor mass increases and resources become scarce.[27,42] As a simulation parameter, the large spread of values of $(D/\rho)_{\text{opt}}$ points toward the same conclusion, that there might not be a universal value for D/ρ describing all cases.

The model favored a high ratio of D_W/D_G. Although it is known that GBM cells tend to be located in white matter and migrate through it, the actual value for the diffusion ratio is not established.[20] One possible reason for the high optimal D_W/D_G favored in this study could be that peritumoral edema often encompassed the GTV. Edema shows a darker intensity on T1 images than white matter, which could be interpreted as gray matter by the FAST segmentation algorithm. Consequently, lowering the diffusion coefficient value of gray matter (increasing the ratio D_W/D_G) may enclose cells in V_0 when there is surrounding edema. The cell diffusion was assumed to be internally isotropic within white matter, even though it is likely that cell migration occurs along the white matter tracts.[47,48] The tract pathways were not available in the form of, for example, diffusion tensor imaging, and were therefore not considered in this study.

In most cases, V was comparable to the volume of V_0 by shape (Fig 2), even though the median value of V_{opt}/V_0 was greater than 2. This was attributed to a "skin-effect," where the total volume may be increased considerably by a surrounding thin voxel layer. The simulation halting condition ensures that V will always be greater than V_0, introducing a bias toward larger volumes. This bias could

possibly be rectified through various means. For example, the halting condition could be more lenient by requiring that only a voxel set fraction reached c = 8000 cells/mm^3 rather than the entire V_0 voxel set. This would help for cases featuring small tumor volumes disconnected from the bulk tumor, because tumor fragments would be excluded from the halting condition, but this entails the risk of disregarding critical tumor data. An alternative halting condition could be to minimize the Hausdorff distance of the 8000 cells/mm^3-isosurface to V_0. However, the aim in this study was to be conservative and to not underestimate extent of the GTV.

In the 3 cases where $V_{opt}/V_0 = 0$, V_0 consisted of multiple tumor volumes, which caused the COM to be placed outside or at the edge of the GTV. Because n_0 was not surrounded by white matter, diffusion was impeded when D/ρ was low, to the degree that $c > k$ after the first diffusion iteration, causing a simulation failure. When D/ρ was increased, the simulations could proceed, though the resulting volumes V were large enough to be deemed outliers. The model might therefore not be perfectly suited for cases with multiple volumes because it assumes a single coherent GTV.

The case with $V_{opt}/V_0 = 0.70$ is controversial because the model should either yield $V/V_0 \geq 1$ or not run at all, yielding a null volume. This value was achieved for a single combination of values for the parameters among the tested ones, D/ρ = 0.1 mm^2 and D_W/D_G = 10, whereas using the other parameter values yielded acceptable values of V/V_0 ranging between 2.63 and 9.51.

The numerical values for the k and n_0 parameters employed in this study have been previously used by Swanson et al[25] and Rockne et al,[26] respectively. As they are not fully established, variation of V_{opt}/V_0 with respect to k and n_0 was investigated while keeping the diffusion and anisotropy parameters constant as $(D/\rho)_{opt}$ and $(D_W/D_G)_{opt}$. The model was robust with respect to k, as the cell concentration tends to be much smaller than k virtually everywhere in the brain except for the innermost parts of V_0. The model was also robust with respect to n_0 for V/V_0, but affected the extent of furthermost spread.

Placement of n_0 in the COM was made in the absence of obvious alternatives. Displacement of the starting voxel from the COM was investigated for few selected cases. As expected, the volume of V increased with displacement distance. The distance to the furthest voxel of V_0 will increase with starting voxel displacement. Thus, V will need to grow larger to encompass V_0.

The simulation halting condition and the volumes of V assumed a visibility threshold of HGG masses on T1 images of 8000 cells/mm^3, as reported by Tracqui et al.[15] Although the value of the visibility threshold affects the extension of tumor invasion, it does not affect the paths of invasion, which are dependent on the distribution of white matter. Pattern of failure was not available in this cohort, and thus could not be used to evaluate the visibility threshold value.

The findings in this study with respect to the CTV delineation can be summarized as follows:

1. The conventional CTV delineation misses tumor concentrations greater than 1 cell/mm^3 in 84% of cases.
2. For the remaining 16% of cases, the CTV delineation overextends into normal tissue.
3. The isotropic extension of the GTV does not render consistent information regarding the density of cells included in this conventionally contoured CTV because of the anisotropy of the predicted tumor invasion.

Very scarce data of the GBM tumor cell distribution in the brain are currently available, thus making a direct model validation not possible at this stage. However, if a large number of cases would become available, a tumor invasion model could be trained using AI methods. The model could then be indirectly verified by correlating model predictions with tumor recurrence or with treatment outcome. An AI-based model could also provide insight into the clinically relevant tumor cell concentration threshold, c_{enc}, for delineating the CTV.

Conclusions

This study presents a model for HGG cell invasion in normal tissue and a methodology for investigating the agreement between the conventionally delineated CTV and the volume invaded by tumor cells. The standard CTV failed to encompass all voxels with tumor cell concentrations equal to or less than 1 cell/mm^3 in 84% of the cases. Calculated Hausdorff distances between the CTV and the volume of tumor invasion indicated poor conformity due to the highly anisotropic pattern of invasion. The presented model may therefore be used in assisting the CTV delineation for HGGs with different levels of diffusivity and anisotropy.

References

1. Ostrom QT, Gittleman H, Truitt G, Boscia A, Kruchko C, Barnholtz-Sloan JS. CBTRUS statistical report: Primary brain and other central nervous system tumors diagnosed in the United States in 2011-2015. *Neuro-Oncol*. 2018;20(suppl_4):iv1–iv86.
2. Sanai N, Alvarez-Buylla A, Berger MS. Neural stem cells and the origin of gliomas. *N Engl J Med*. 2005;353:811–822.
3. DeLuca P, Jones D, Gahbauer R, Whitmore G, Wambersie A. Prescribing, recording, and reporting photon-beam intensity-modulated radiation therapy (IMRT): Contents. *J Int Comm Radiat Units Meas*. 2010;10:1–3.
4. McKenzie AL, van Herk M, Mijnheer B. The width of margins in radiotherapy treatment plans. *Phys Med Biol*. 2000;45:3331–3342.

5. Hochberg FH, Pruitt A. Assumptions in the radiotherapy of glioblastoma. *Neurology*. 1980;30:907–911.
6. Wallner KE, Galicich JH, Krol G, Arbit E, Malkin MG. Patterns of failure following treatment for glioblastoma multiforme and anaplastic astrocytoma. *Int J Radiat Oncol Biol Phys*. 1989;16:1405–1409.
7. Brandes AA, Tosoni A, Franceschi E, et al. Recurrence pattern after temozolomide concomitant with and adjuvant to radiotherapy in newly diagnosed patients with glioblastoma: Correlation with MGMT promoter methylation status. *J Clin Oncol*. 2009;27:1275–1279.
8. Ogura K, Mizowaki T, Arakawa Y, et al. Initial and cumulative recurrence patterns of glioblastoma after temozolomide-based chemoradiotherapy and salvage treatment: A retrospective cohort study in a single institution. *Radiat Oncol*. 2013;8:97.
9. Stupp R, Mason WP, van den Bent MJ, et al. Radiotherapy plus concomitant and adjuvant temozolomide for glioblastoma. *N Engl J Med*. 2005;352:987–996.
10. Colman H, Berkey BA, Maor MH, et al. Phase II Radiation Therapy Oncology Group trial of conventional radiation therapy followed by treatment with recombinant interferon-beta for supratentorial glioblastoma: Results of RTOG 9710. *Int J Radiat Oncol Biol Phys*. 2006;66:818–824.
11. Liang BC, Thornton AFJ, Sandler HM, Greenberg HS. Malignant astrocytomas: Focal tumor recurrence after focal external beam radiation therapy. *J Neurosurg*. 1991;75:559–563.
12. Burger PC, Heinz ER, Shibata T, Kleihues P. Topographic anatomy and CT correlations in the untreated glioblastoma multiforme. *J Neurosurg*. 1988;68:698–704.
13. Silbergeld DL, Chicoine MR. Isolation and characterization of human malignant glioma cells from histologically normal brain. *J Neurosurg*. 1997;86:525–531.
14. Yamahara T, Numa Y, Oishi T, et al. Morphological and flow cytometric analysis of cell infiltration in glioblastoma: A comparison of autopsy brain and neuroimaging. *Brain Tumor Pathol*. 2010;27:81–87.
15. Tracqui P, Cruywagen GC, Woodward DE, Bartoo GT, Murray JD, Alvord Jr EC. A mathematical model of glioma growth: The effect of chemotherapy on spatio-temporal growth. *Cell Prolif*. 1995;28:17–31.
16. Swanson KR. *Mathematical Modeling of the Growth and Control of Tumors*. Seattle, WA: University of Washington; 1999.
17. Harpold H, Alvord E, Swanson K. The evolution of mathematical modeling of glioma proliferation and invasion. *J Neuropathol Exp Neurol*. 2007;66:1–9.
18. Alfonso JCL, Talkenberger K, Seifert M, et al. The biology and mathematical modelling of glioma invasion: A review. *J R Soc Interface*. 2017:14.
19. Woodward DE, Cook J, Tracqui P, Cruywagen GC, Murray JD, Alvord ECJ. A mathematical model of glioma growth: The effect of extent of surgical resection. *Cell Prolif*. 1996;29:269–288.
20. Swanson KR, Alvord ECJ, Murray JD. A quantitative model for differential motility of gliomas in grey and white matter. *Cell Prolif*. 2000;33:317–329.
21. Lazzeroni M, Manesh ZK, Sandström H, Barsoum P, Toma-Dasu I. Impact of tumour cell infiltration on treatment outcome in gamma knife radiosurgery: A modelling study. *Anticancer Res*. 2019;39:1675–1687.
22. Jbabdi S, Mandonnet E, Duffau H, et al. Simulation of anisotropic growth of low-grade gliomas using diffusion tensor imaging. *Magn Reson Med*. 2005;54:616–624.
23. Clatz O, Sermesant M, Bondiau PY, et al. Realistic simulation of the 3-D growth of brain tumors in MR images coupling diffusion with biomechanical deformation. *IEEE Trans Med Imaging*. 2005;24:1334–1346.
24. Unkelbach J, Menze BH, Konukoglu E, et al. Radiotherapy planning for glioblastoma based on a tumor growth model: Improving target volume delineation. *Phys Med Biol*. 2014;59:747–770.
25. Swanson KR, Rockne RC, Claridge J, Chaplain MA, Alvord ECJ, Anderson ARA. Quantifying the role of angiogenesis in malignant progression of gliomas: In silico modeling integrates imaging and histology. *Cancer Res*. 2011;71:7366–7375.
26. Rockne R, Rockhill JK, Mrugala M, et al. Predicting the efficacy of radiotherapy in individual glioblastoma patients in vivo: A mathematical modeling approach. *Phys Med Biol*. 2010;55:3271–3285.
27. Stensjoen AL, Solheim O, Kvistad KA, Haberg AK, Salvesen O, Berntsen EM. Growth dynamics of untreated glioblastomas in vivo. *Neuro-Oncol*. 2015;17:1402–1411.
28. Menze BH, Jakab A, Bauer S, et al. The multimodal brain tumor image segmentation benchmark (BRATS). *IEEE Trans Med Imaging*. 2015;34:1993–2024.
29. Bakas S, Akbari H, Sotiras A, et al. Advancing The Cancer Genome Atlas glioma MRI collections with expert segmentation labels and radiomic features. *Sci Data*. 2017;4: 170117.
30. Bakas S, Reyes M, Jakab A, et al. Identifying the best machine learning algorithms for brain tumor segmentation, progression assessment, and overall survival prediction in the BRATS challenge. *ArXiv*. 2018. abs/1811.02629.
31. Bakas S, Akbari H, Sotiras A, et al. Segmentation labels and radiomic features for the pre-operative scans of the TCGA-GBM collection. 2017. Available at: https://wiki.cancerimagingarchive.net/pages/viewpage.action?pageId=24282666. Accessed April 30, 2018.
32. Astaraki M, Wang C, Carrizo G, Toma-Dasu I, Smedby Ö. Multimodal brain tumor segmentation with normal appearance autoencoder. *Lecture Notes in Computer Science (Including Subseries Lecture Notes in Artificial Intelligence and Lecture Notes in Bioinformatics)*. Springer; 2020:316–323.
33. Astaraki M, Toma-Dasu I, Smedby Ö, Wang C. Normal appearance autoencoder for lung cancer detection and segmentation. *Medical Image Computing and Computer Assisted Intervention - MICCAI 2019 - 22nd International Conference, Shenzhen, China, October 13-17, 2019, Proceedings, Part VI*. Shenzhen, China: Springer; 2019:249–256.
34. Ronneberger O, Fischer P, Brox T. U-Net: Convolutional networks for biomedical image segmentation. In: Navab N, Hornegger J, Wells WM, Frangi AF, eds. *Medical Image Computing and Computer-Assisted Intervention − MICCAI 2015*. Munich, Germany: Springer International Publishing; 2015:234–241.
35. Zhang Y, Brady M, Smith S. Segmentation of brain MR images through a hidden Markov random field model and the expectation-maximization algorithm. *IEEE Trans Med Imaging*. 2001;20:45–57.
36. Murray JD. *Mathematical Biology*. 19. Berlin Heidelberg: Springer-Verlag; 1989.
37. Cook J, Woodward D, Tracqui P, Murray J. Resection of gliomas and life expectancy. *J Neuro-Oncol*. 1995;24:131–135.
38. Burgess PK, Kulesa PM, Murray JD, Alvord Jr EC. The interaction of growth rates and diffusion coefficients in a three-dimensional mathematical model of gliomas. *J Neuropathol Exp Neurol*. 1997;56:704–713.
39. Yee K. Numerical solution of initial boundary value problems involving maxwell's equations in isotropic media. *IEEE Trans Antennas Propag*. 1966;14:302–307.
40. Krishnan V, Lim TC, Ho FCH, Peh WC. Clinics in diagnostic imaging (175). Corpus callosum glioblastoma multiforme (GBM): Butterfly glioma. *Singapore Med J*. 2017;58:121–125.
41. Swanson KR, Rostomily RC, Alvord EC. A mathematical modelling tool for predicting survival of individual patients following resection of glioblastoma: A proof of principle. *Br J Cancer*. 2008;98:113–119.
42. Rutter EM, Stepien TL, Anderies BJ, et al. Mathematical analysis of glioma growth in a murine model. *Sci Rep*. 2017;7:2508.
43. Dice LR. Measures of the amount of ecologic association between species. *Ecology*. 1945;26:297–302.
44. Shusharina N, Söderberg J, Edmunds D, Löfman F, Shih H, Bortfeld T. Automated delineation of the clinical target volume using anatomically constrained 3D expansion of the gross tumor volume. *Radiother Oncol J Eur Soc Ther Radiol Oncol*. 2020;146:37–43.
45. Duma CM, Kim BS, Chen PV, et al. Upfront boost gamma knife "leading-edge" radiosurgery to FLAIR MRI-defined tumor

migration pathways in 174 patients with glioblastoma multiforme: A 15-year assessment of a novel therapy. *J Neurosurg*. 2016;125:40–49.
46. Valverde S, Oliver A, Cabezas M, Roura E, Lladó X. Comparison of 10 brain tissue segmentation methods using revisited IBSR annotations. *J Magn Reson Imaging*. 2015;41:93–101.
47. Giese A, Kluwe L, Laube B, Meissner H, Berens ME, Westphal M. Migration of human glioma cells on myelin. *Neurosurgery*. 1996;38:755–764.
48. Demuth T, Berens ME. Molecular mechanisms of glioma cell migration and invasion. *J Neurooncol*. 2004;70:217–228.